

# Analysis of the light scattering properties of a gold nanorod on a plane surface via discrete sources method

Elena Eremina <sup>a,\*</sup>, Yuri Eremin <sup>b,1</sup>, Thomas Wriedt <sup>c,2</sup>

<sup>a</sup> *Universitaet Bremen, Badgasteiner Str. 3, 28359 Bremen, Germany*

<sup>b</sup> *Faculty of Applied Mathematics and Computer Science, Moscow State University, Lenin's Hills, 119992 Moscow, Russia*

<sup>c</sup> *Institut für Werkstofftechnik, Badgasteiner Str. 3, 28359 Bremen, Germany*

Received 26 September 2006; received in revised form 1 December 2006; accepted 4 December 2006

## Abstract

The Discrete Sources Method has been extended to analyze the scattering behavior of a gold nanorod deposited on a plane surface in an evanescent wave field. In this case the system particle-surface demonstrates no axial symmetry and it is not possible to apply the conventional DSM approach for axisymmetric systems used before. In this paper DSM algorithm for non-axisymmetric systems is presented. The rigorous computer model based on DSM, which allows to take into account all features of the scattering problem including particle-surface interaction has been realized. Computer simulation analysis of the scattering spectra of gold nanorod is presented.

© 2006 Elsevier B.V. All rights reserved.

*Keywords:* Evanescent light scattering; Nanorod; Discrete sources method

## 1. Introduction

Noble metal nanoparticles attracted great interest in recent years due to their special properties in optical scale [1]. Nowadays nanoparticles have practical value in many applications such as chemical and biochemical sensors, medical diagnostics and therapeutics, biological imaging, nanophotonics etc. [2–6]. When the dimension of a metal nanoparticle is small enough compared to the wavelength of incident light, surface plasmon can be excited due to a collective motion of free electrons at the surface of the metal nanoparticle that resonantly couples with the oscillating electric field of the light. As a result of surface plasmon excitation, strong enhancements of absorption, scattering, and local electric field in the vicinity of particle

and in far zone arise. This effect strongly depends on particle size, shape, and type of materials, excitation and the local environment [7–9]. This is the key feature for their applications. Optical absorption and scattering have dominant effects at different size regions, which can be used in certain applications. The dependence of the Plasmon resonance on the surrounding medium is useful in imaging methods to detect attached biosystems [2].

In general, optical scattering effects, significant for particles larger than a few tens of nanometers, gives a more efficient detection scheme for monitoring the local environments of single particle Plasmon resonance. For sensor and other applications it is very important to understand how the optical absorption and scattering depend on the particle geometry, material and excitation to find a way to control their relative contribution for the selected application. From the viewpoint of optical scattering, noble metal nanorods have attracted additional attention due to their higher tunability of resonance frequency and multiple resonance peaks in compare with spherical particles [10]. Even small elongation of spherical nanoparticle demonstrates

\* Corresponding author. Tel.: +49 421 218 3583; fax: +49 421 218 5378.

E-mail addresses: [eremina@iwt.uni-bremen.de](mailto:eremina@iwt.uni-bremen.de) (E. Eremina), [eremin@cs.msu.su](mailto:eremin@cs.msu.su) (Y. Eremin), [thw@iwt.uni-bremen.de](mailto:thw@iwt.uni-bremen.de) (T. Wriedt).

<sup>1</sup> Tel./fax: +7 095 939 1776.

<sup>2</sup> Tel.: +49 421 218 3583; fax: +49 421 218 2507.



$\partial D_i$ . Only the amplitudes of discrete sources are to be determined from the boundary conditions at the particle surface, which can be rewritten in following form

$$\mathbf{n}_p \times (\mathbf{E}_i - \mathbf{E}_0^s) = \mathbf{n}_p \times \mathbf{E}_0^0; \quad \mathbf{n}_p \times (\mathbf{H}_i - \mathbf{H}_0^s) = \mathbf{n}_p \times \mathbf{H}_0^0, \quad (2)$$

where  $\{\mathbf{E}_0^0, \mathbf{H}_0^0\}$  is the transmitted plane wave inside  $D_0$ .

To construct the fields scattered by a particle we will use system of localized dipoles [20]. The field of dipoles analytically satisfy the transmission conditions for tangential components of electric and magnetic fields enforced at the plane interface  $\Sigma$ . In this case the vector potential accepts the form

$$\mathbf{A}(M) = \int_V \vec{\mathbf{G}}(M, M_0) \mathbf{j}(P) d\tau_P, \quad (3)$$

where  $\vec{\mathbf{G}}(M, M_0)$  is the Green Tensor of a half-space [16]:

$$\vec{\mathbf{G}}(M, M_0) = \begin{bmatrix} G_{11} & 0 & 0 \\ 0 & G_{11} & 0 \\ \frac{\partial g}{\partial x_M} & \frac{\partial g}{\partial y_M} & G_{33} \end{bmatrix}. \quad (4)$$

The corresponding tensor components can be written as

$$G_{\alpha\alpha}(M, M_0) = \frac{k_0}{j} h_0^{(2)}(k_0 R_{MM_0}) + \int_0^\infty J_0(\lambda r) v_{\alpha\alpha}(\lambda, z) \times \exp\{-\eta_0 z\} \lambda d\lambda, \quad \alpha = 1, 3 \quad (5)$$

$$g(M, M_0) = \int_0^\infty J_0(\lambda r) v_{31}(\lambda, z_0) \exp\{-\eta_0 z\} \lambda d\lambda.$$

Here  $R_{MM_0} = r^2 + (z - z_0)^2 r^2 = \rho^2 + \rho_0^2 - 2\rho\rho_0 \cos(\varphi - \varphi_0) J_0(\cdot)$  is the cylindrical Bessel function,  $h_0^{(2)}$  is the spherical Hankel function,  $(\rho_0, \varphi_0, z_0)$  are the cylindrical coordinates of the point  $M_0$  of multipoles. The associating spectral functions  $v_{11}, v_{33}, v_{31}$  are given by

$$v_{11}(\lambda, z, z_0) = \frac{\mu_1 \eta_0 - \mu_0 \eta_1}{\mu_1 \eta_0 + \mu_0 \eta_1} \frac{1}{\eta_0} \exp\{-\eta_0 z_0\};$$

$$v_{33}(\lambda, z, z_0) = \frac{\varepsilon_1 \eta_0 - \varepsilon_0 \eta_1}{\varepsilon_1 \eta_0 + \varepsilon_0 \eta_1} \frac{1}{\eta_0} \exp\{-\eta_0 z_0\} \quad z \geq 0, \quad z_0 > 0;$$

$$v_{31}(\lambda, z, z_0) = \frac{2(\mu_1 \varepsilon_1 - \mu_0 \varepsilon_0)}{(\mu_1 \eta_0 + \mu_0 \eta_1)(\varepsilon_1 \eta_0 + \varepsilon_0 \eta_1)} \exp\{-\eta_0 z_0\}, \quad (6)$$

where  $\eta_\zeta^2 = \lambda^2 - k_\zeta^2$ ,  $k_\zeta^2 = k^2 \varepsilon_\zeta \mu_\zeta$ ,  $\zeta = 0, 1$ .

We will construct the representation for the scattered fields in  $D_{0,1}$  basing on a system of electric dipoles, deposited in some points  $M_n$ . Let  $\{M_n\}_{n=1}^\infty$  is a dense set of points, which are distributed over an auxiliary surface  $S_0 \in C^{(2,\alpha)}$  localized inside  $D_i$  and co-axed with  $\partial D_i$  (Fig. 1). Let us consider three linearly independent electric dipoles  $\{\mathbf{e}^l\}_{l=1}^3$  situated in every point  $M_n$  and orientated in accordance with the cylindrical coordinate system. Following (3) the corresponding potentials for these dipoles take a form:

$$\mathbf{A}_n^1 = \{G_{11}(M, M_n) \cos(\varphi - \varphi_n); \quad -G_{11} \sin(\varphi - \varphi_n);$$

$$\frac{\partial g(M, M_n)}{\partial \rho} \cos(\varphi - \varphi_n) - \frac{1}{\rho} \frac{\partial g}{\partial \varphi} \sin(\varphi - \varphi_n)\};$$

$$\mathbf{A}_n^2 = \{G_{11}(M, M_n) \sin(\varphi - \varphi_n); \quad G_{11} \cos(\varphi - \varphi_n); \quad (7)$$

$$\frac{\partial g(M, M_n)}{\partial \rho} \sin(\varphi - \varphi_n) + \frac{1}{\rho} \frac{\partial g}{\partial \varphi} \cos(\varphi - \varphi_n)\};$$

$$\mathbf{A}_n^3 = \{0; 0; G_{33}(M, M_n)\}.$$

Then for the scattered fields in  $D_{0,1}$  which satisfy the transmission conditions at  $\Sigma$ , the following representation is valid:

$$\mathbf{E}_\zeta^N(M) = \sum_{n=1}^{N_0} \sum_{l=1}^3 p_{nl}^0 \text{rot rot } \mathbf{A}_n^l(M),$$

$$\mathbf{H}_\zeta^N(M) = \frac{j}{k\mu} \text{rot } \mathbf{E}_\zeta^N(M), \quad \zeta = 0, 1; \quad M \in D_{0,1}. \quad (8)$$

Let us emphasize that the scattered fields in  $D_0$  and  $D_1$  are represented by an unitary set of dipoles' amplitudes  $\{p_{nl}^0\}$ .

Consider now the construction of the approximated solution for the total field inside a particle  $D_i$ . We will choose the co-axial surface  $S_i$ , which confines  $\partial D_i$  (Fig. 1), and a dense set of points  $\{M_n\}_{n=1}^\infty$ , which are distributed over  $S_i$ . Let us introduce the following system of vector potentials corresponding to the external electrical dipoles:

$$\mathbf{A}_{ni}^l(M) = h_0^{(2)}(k_i R_{MM_i}) \mathbf{e}_l; \quad M_n \in S_i.$$

Then the representation for the total field inside the particle accepts the form:

$$\mathbf{E}_i^N(M) = \sum_{n=1}^{N_i} \sum_{l=1}^3 p_{ni}^l \text{rot rot } \mathbf{A}_{ni}^l(M),$$

$$\mathbf{H}_i^N(M) = \frac{j}{k\mu_i} \text{rot } \mathbf{E}_i^N(M), \quad M \in D_i. \quad (9)$$

The representation for internal field (9) essentially differs from those presented in [21]. Deposition of  $S_i$  outside  $D_i$  region seems to be more efficient especially for metal particles of small diameter. The representations (8), (9) satisfy all the conditions of the boundary value problem (1) except the boundary conditions enforced at a particle surface  $\partial D_i$ . Unknown amplitudes of the discrete sources are to be defined from (2). Because the representation for the scattered field (8) satisfies the transmission conditions for the fields at the interface  $\Sigma$ , it allows to take into account all interactions between particle and prism surface analytically.

The completeness of the system of dipoles guarantees the convergence of the approximate solution to the exact one [16].

### 3. Numerical scheme of the DSM

In this section, we describe the details of our numerical scheme, which was realized from the new DSM based

model of the last section. We also focus on the differences between the new model and the conventional one [16].

As has been mentioned, the approximate DSM solution (8), (9) satisfies most of the conditions of the scattering problem (1). So, the determination of the unknown amplitudes of discrete sources  $\{\{p_{nl}^0\}_{n=1}^{N_0}\}_{l=1}^3; \{\{p_{nl}^i\}_{n=1}^{N_i}\}_{l=1}^3\}$  is to be performed from the fitting of the boundary conditions (2) enforced at the particle surface  $\partial D_i$  in  $L_2(\partial D_i)$  norm [16]. To do this, we need an expression for the exciting field  $\{\mathbf{E}_0^0, \mathbf{H}_0^0\}$  in the  $D_0$  domain. In our case the refracted field in  $D_0$  takes the form

$$\mathbf{E}_0^0 = T^{P,S} \mathbf{e}^{P,S} \exp(-i\mathbf{k}r), \quad \mathbf{H}_0^0 = n_0 \mathbf{k} \times \mathbf{E}_0^0; \quad (10)$$

here  $\mathbf{k} = (-\sin \theta_1 \cos \varphi_1; -\sin \theta_1 \sin \varphi_1; -\cos \theta_1)^T$ ;

$$\mathbf{e}^P = (-\cos \theta_1 \cos \varphi_1; -\cos \theta_1 \sin \varphi_1; \sin \theta_1)^T;$$

$$\mathbf{e}^S = (\sin \varphi_1; -\cos \varphi_1; 0)^T;$$

$$T^P = \frac{2n_1 \cos \theta_1}{n_0 \cos \theta_1 + n_1 \cos \theta_0}; \quad T^S = \frac{2n_1 \cos \theta_1}{n_1 \cos \theta_1 + n_0 \cos \theta_0};$$

$n_\zeta = \sqrt{\varepsilon_\zeta \mu_\zeta}$  is a refractive index in  $D_\zeta$ ,  $\theta_0$  is a refraction angle of the wave transmitted into  $D_0$ .

Various schemes for the amplitude determination are at our disposal. It has been established that more stable results can be obtained by using pseudo-inversion of an over-determined system of linear equations obtained by following the generalized point-matching technique. Select a set of matching points on the particle,  $\{P_j\}_{j=1}^J \in \partial D_i$ , homogeneously covering the scatterer's surface  $\partial D_i$ . Then the linear system to be used for determining the discrete sources amplitudes can be found from matching the boundary conditions (2) at the set  $\{P_j\}_{j=1}^J$ . This procedure leads to an over determined linear system with a dimension of  $4J \times 3(N_0 + N_i)$ . The discrete sources amplitudes are evaluated by a pseudo inversion technique [22]. The DSM scheme enables an estimation of the error in the solution by calculating of the surface residual in  $L_2(\partial D_i)$  norm. Completeness of the dipoles system provides convergence of the approximate solution (8), (9) to the exact solution of the scattering problem (1) [21].

Let us emphasize the main differences between the new DSM scheme and the conventional DSM one applied to axial symmetric structures on a substrate [16].

1. The approximate solution (8), (9) is independent of the polarization of the external excitation in contrast to the conventional DSM [16]. This allows examination of the scattering problem for the whole set of polarizations and incident angles at once.
2. The representation for the scattered field (9) involves the dipole sources only. It simplifies the numerical evaluation of the Sommerfeld integrals (5), and provides a more stable scheme for the matrix elements computation compared to the conventional DSM where multipole sources are used [16].

The number of matching points where the DS amplitudes are defined increases until the necessary accuracy of the results is achieved. The DS number usually is 4–6 times less then the number of matching points. Resulting errors are estimated by computation of a surface residual in least-square norm. As a rule in a range of parameters under consideration relative surface residual less then 0.2% assures the results errors to be less then 0.1%.

After the amplitudes of the discrete sources are determined, one can calculate the far field pattern  $\mathbf{F}(\theta, \varphi)$  of the scattered field, which is determined at the upper part of the unite semi-sphere  $\Omega = \{0^\circ \leq \theta < 90^\circ, 0^\circ \leq \phi \leq 360^\circ\}$  and is given by

$$\mathbf{E}(M)/|\mathbf{E}_0^0(z=0)| = \frac{\exp\{-ik_0 r\}}{r} \mathbf{F}(\theta, \varphi) + O(1/r^2),$$

$$r = |M| \rightarrow \infty, \quad z > 0.$$

We use an asymptotic approximation for the Sommerfeld integrals [22], which leads to the following representation for the components of the scattering diagram

$$F_\theta(\theta_1, \theta, \varphi) = ik \sum_{n=1}^{N_0} \{P_{n1}^0 f_{\theta 1} + P_{n2}^0 f_{\theta 2} - P_{n3}^0 f_{\theta 3}\},$$

$$F_\varphi(\theta_1, \theta, \varphi) = ik \sum_{n=1}^{N_0} \{-P_{n1}^0 f_{\varphi 1} + P_{n2}^0 f_{\varphi 2}\}.$$

$$f_{\theta 1} = \cos \theta \cos(\varphi - \varphi_n) \gamma^+ + \{\cos \theta \bar{v}_{11}(\theta) + \sin^2 \theta \bar{v}_{33}(\theta)\} \cos \theta \cos(\varphi - \varphi_n) \gamma^-,$$

$$f_{\theta 2} = \cos \theta \sin(\varphi - \varphi_n) \gamma^+ + \{\cos \theta \bar{v}_{11}(\theta) + \sin^2 \theta \bar{v}_{33}(\theta)\} \cos \theta \sin(\varphi - \varphi_n) \gamma^-,$$

$$f_{\theta 3} = \sin \theta \gamma^+ + \cos \theta \bar{v}_{33}(\theta) \sin \theta \gamma^-,$$

$$f_{\varphi 1} = \sin(\varphi - \varphi_n) \gamma^+ + \cos \theta \bar{v}_{11}(\theta) \sin(\varphi - \varphi_n) \gamma^-,$$

$$f_{\varphi 2} = \cos(\varphi - \varphi_n) \gamma^+ + \cos \theta \bar{v}_{11}(\theta) \cos(\varphi - \varphi_n) \gamma^-;$$

$$\gamma^+ = \exp\{ik_0(\rho_n \sin \theta \cos(\varphi - \varphi_n) + z_n \cos \theta)\};$$

$$\gamma^- = \exp\{ik_0(\rho_n \sin \theta \cos(\varphi - \varphi_n) - z_n \cos \theta)\}.$$

(11)

Here  $(\rho_n, \varphi_n, z_n)$  are the cylindrical coordinates of the points  $M_n \in S_0$ . Spectral functions involved into representation (11) accept the form

$$\bar{v}_{11}(\theta) = \frac{2\mu_0}{\mu_1 \cos \theta + \mu_0 \psi}, \quad \psi = \sqrt{\varepsilon_1 - \sin^2 \theta},$$

$$\bar{v}_{33}(\theta) = \frac{2\varepsilon_0}{\varepsilon_1 \cos \theta + \varepsilon_0 \psi},$$

$$\bar{v}_{31}(\theta) = \frac{2(\mu_1 \varepsilon_1 - \mu_0 \varepsilon_0)}{(\varepsilon_1 \cos \theta + \varepsilon_0 \psi)(\mu_1 \cos \theta + \mu_0 \psi)}.$$

Hence, the components of the far field pattern (11) do not contain Sommerfeld integrals and can be represented as finite linear combinations of elementary functions. This circumstance ensures a low costs computation of the scattering characteristics in the far zone.

**4. Results and discussion**

In the paper we will consider the intensity of scattered unpolarized light

$$I(\theta_1, \theta, \varphi) = \frac{1}{2} (|I^P(\theta_1, \theta, \varphi)|^2 + |I^S(\theta_1, \theta, \varphi)|^2), \tag{12}$$

where  $I^{P,S}(\theta_1, \theta, \varphi) = |F_{\theta}^{P,S}(\theta_1, \theta, \varphi)|^2 + |F_{\phi}^{P,S}(\theta_1, \theta, \varphi)|^2$  and  $F_{\theta,\phi}^{P,S}(\theta_1, \theta, \varphi)$  are the components of the far field pattern for P and S polarized incident plane wave in a spherical coordinate system  $\theta, \varphi$ . We are mainly interested in the objective scattering cross-section (objective response), which represents the integrated intensity scattered into the prescribed solid angle  $\Omega$

$$\sigma(\lambda) = \int_{\Omega} I(\theta_1, \theta, \varphi) d\omega, \tag{13}$$

where  $\Omega = \{0 \leq \theta \leq 34^\circ; 0 \leq \varphi \leq 360^\circ\}$ , which corresponds the Numerical Aperture of the objective lens  $NA = 0.75$ .

As a shape model of nanorod we consider an elongated spheroid with equivolume diameter equal to 40 nm. As nanorod material we took gold (Au) and as substrate material BK7 glass. As incidence an unpolarized light has been taken. An incident angle was chosen at  $\theta = 63^\circ$  which is very close to the critical angle  $\theta_c = \arcsin(n_0/n_1)$ . We remind that  $n_0, n_1$  depend on the exciting wavelength  $\lambda$ , and  $\theta = 0^\circ$  corresponds to the normal direction to the prism surface. We also examined different orientations of the spheroid with respect to the incident plane. In the results presented below the  $\varphi = 180^\circ$  plane corresponds to the incidence case where P-polarized  $E$  belongs to the  $zx$ -plane and  $\varphi = 90^\circ$  plane corresponds to the incidence case when P-polarized  $E$  belongs to the  $zy$ -plane.

In Fig. 2 the objective response (13) versus wavelength for a spheroid with aspect ratio  $a = 1.5$  and different orientations is compared to the objective response for a sphere.

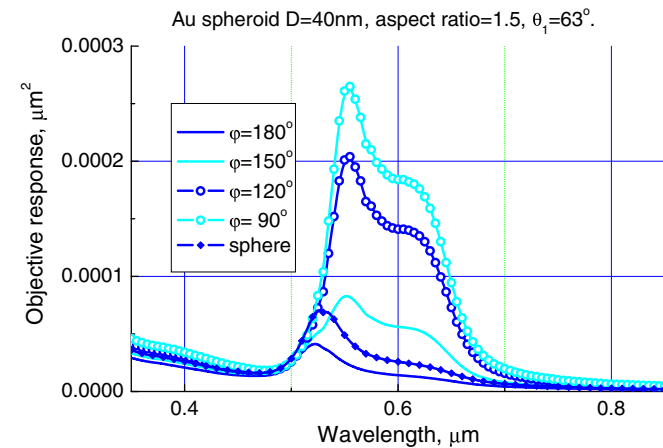


Fig. 2. The objective response (13) versus wavelength for a gold (Au) spheroid of diameter  $D = 40$  nm and aspect ratio  $a = 1.5$  for different orientations of the incident plane compared to the objective response for an equivolume sphere.

From the results one can see, that the objective response from a spheroid in case of  $\varphi = 180^\circ$  is lower than one from a sphere. Objective responses for spheroids with  $a = 2$  and  $a = 2.5$  are presented in Figs. 3 and 4 respectively. From comparison of results it is obvious, that maximum enhancement of objective response for spheroid is reached at  $\varphi = 90^\circ$  and lowest – at  $\varphi = 180^\circ$ . Besides, the spectral peak shifts to the area of longer wavelengths when aspect ratio of spheroid increases.

Let us now fix the incident plane and vary the aspect ratio of the spheroid. Fig. 5 shows an objective response versus wavelength for  $\varphi = 180^\circ$ . In Figs. 6 and 7 similar results are presented for  $\varphi = 150^\circ$  and  $\varphi = 90^\circ$ , respectively. From Fig. 5 we can see that for  $\varphi = 180^\circ$  the objective response for a sphere exceeds the one from a spheroid. But with rotation of the incidence plane from  $180^\circ$  to  $90^\circ$  the objective response of a spheroid gets higher (Figs. 6 and 7). The objective response from a spheroid mostly exceeds the objective response from a sphere. From a range

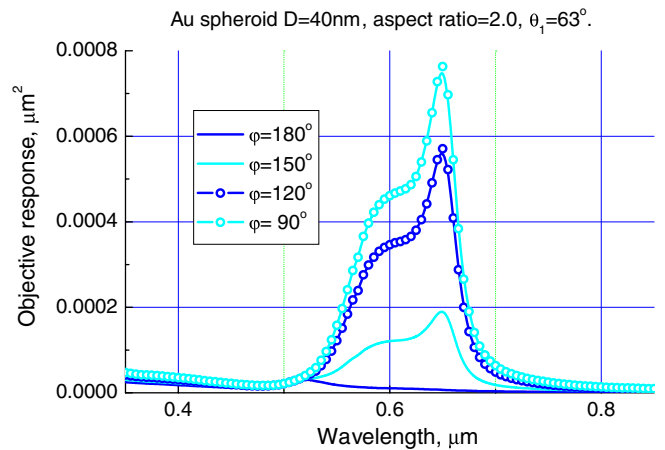


Fig. 3. The objective response versus wavelength for a gold spheroid of aspect ratio  $a = 2$ , different orientations of the incident plane.

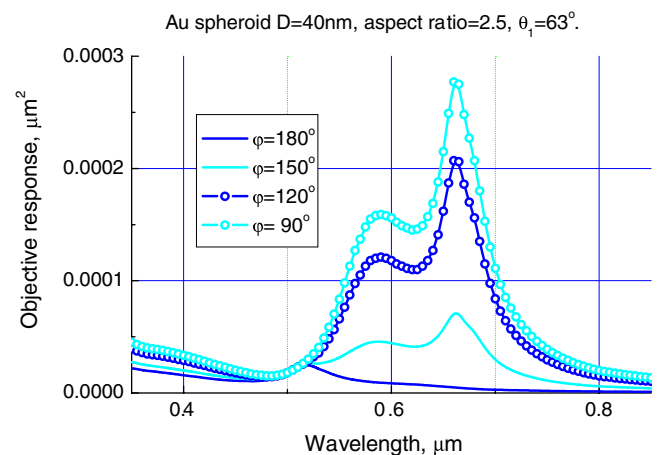


Fig. 4. The objective response versus wavelength for a gold spheroid of aspect ratio  $a = 2.5$ , different orientations of the incident plane.

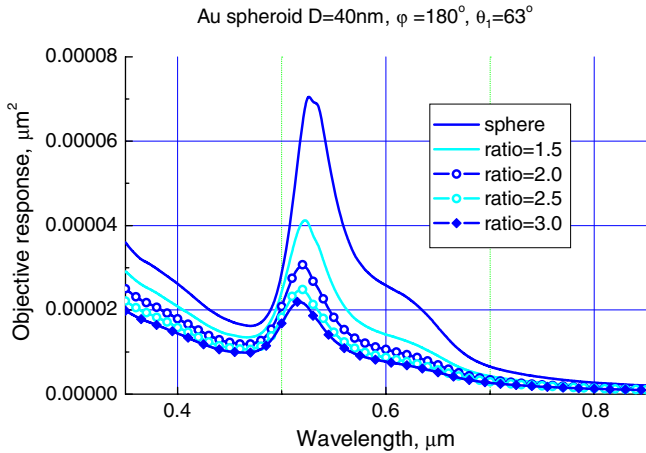


Fig. 5. The objective response versus wavelength for different aspect ratios of a gold spheroid compared to the one from a sphere for the incident plane orientation  $\varphi = 180^\circ$ .

of aspect ratios only a spheroid with  $a = 3$  demonstrates lower response (Fig. 6). In Fig. 6 we see, that a spheroid with  $a = 2$  provides a maximum enhancement in the objec-

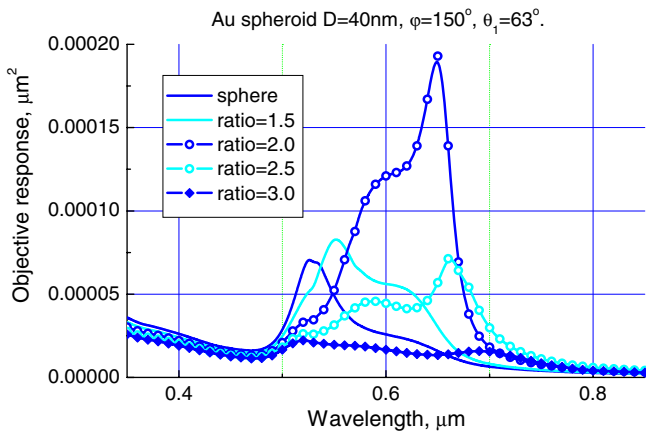


Fig. 6. The objective response versus wavelength for different aspect ratios of a gold spheroid compared to the one from a sphere for  $\varphi = 150^\circ$ .

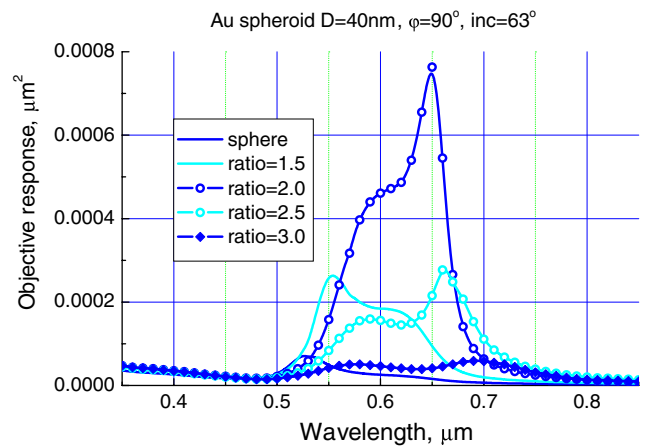


Fig. 7. The objective response versus wavelength for different aspect ratios of a gold spheroid compared to the one from a sphere for  $\varphi = 90^\circ$ .

tive response among the others. Fig. 8 presents more detailed investigation in aspect ratio range close to 2. Again from the results we see that maximum of response is reached with an aspect ratio of 2.

Let us now investigate what happens with the scattering intensity of unpolarised light (12) when the objective response reaches its maximum value. In Fig. 9 the scattering intensity versus scattering angle for a spheroid of  $a = 1.5$  for different orientations of incident plane is presented. For demonstration we took  $\lambda = 550$  nm corresponding to the resonance peak of this spheroid. Similar results for a spheroid of  $a = 2$  and  $\lambda = 650$  nm are presented in Fig. 10. From results analysis of the results one can notice that intensity gets higher with rotation of the incidence plane from  $180^\circ$  to  $90^\circ$ .

Now we would like to investigate which polarization is responsible for the intensity enhancement. For this aim a spheroid of  $a = 2$  is taken.

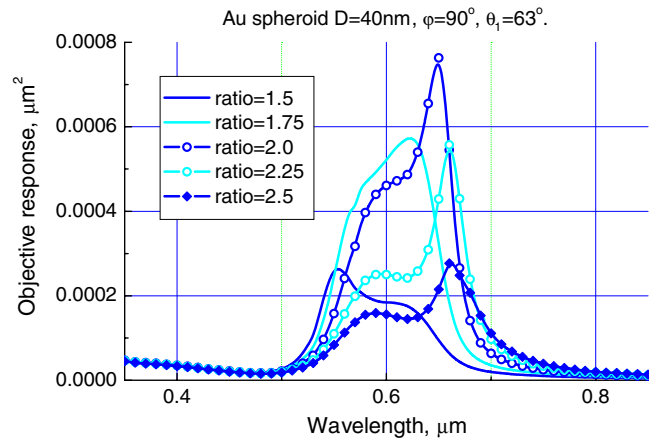


Fig. 8. The objective response versus wavelength for different aspect ratios of a gold spheroid compared to the one from a sphere for  $\varphi = 90^\circ$  for the smaller step of aspect ratios.

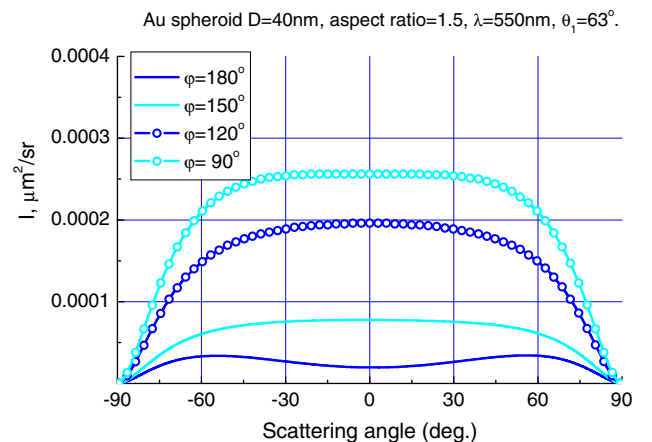


Fig. 9. The scattering intensity versus scattering angle for a spheroid of  $a = 1.5$  for different orientations of the incident plane, and wavelength  $\lambda = 550$  nm.

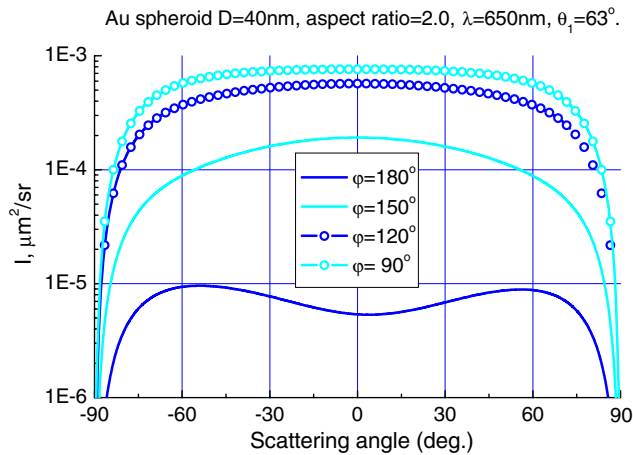


Fig. 10. The scattering intensity versus scattering angle for a spheroid of  $a = 2$  for different orientations of the incident plane,  $\lambda = 650$  nm.

In Fig. 11 the intensity of the polarized light versus scattering angle for such a spheroid for two positions of the incident plane and  $\lambda = 650$  nm is presented. One can see that curves for P-polarized light do not depend so much on the orientation of the incident plane, but for S-polarization its intensity drastically increases with a rotation of the incidence plane from  $180^\circ$  to  $90^\circ$ . Thus, the main contribution into intensity is mostly provided by the S-component. In Fig. 12 the intensity of S-polarized light versus scattering angle is presented for spheroids of aspect ratios close to 2 with a small step. From these results one can notice that the intensity is maximal for  $a = 2$  which helps to explain results from Figs. 6–8.

Finally we would like to summarise our research using computer simulation:

1. The spectral peak shifts to the area of longer wavelengths with increasing aspect ratio of a spheroid;

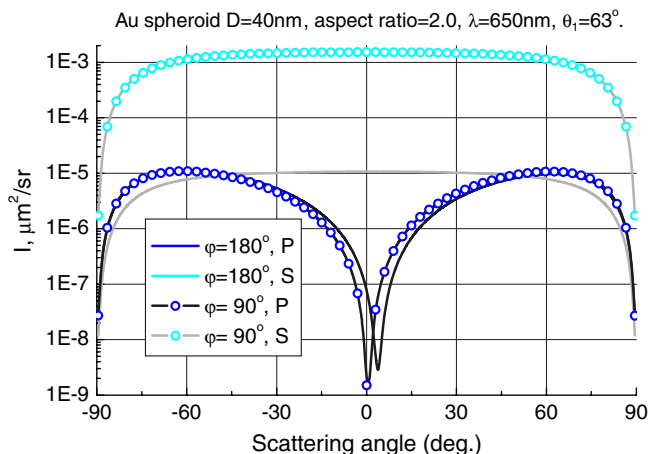


Fig. 11. The scattering intensity of P and S-polarized components versus scattering angle for a spheroid of  $a = 2$  for different orientations of the incident plane,  $\lambda = 650$  nm.

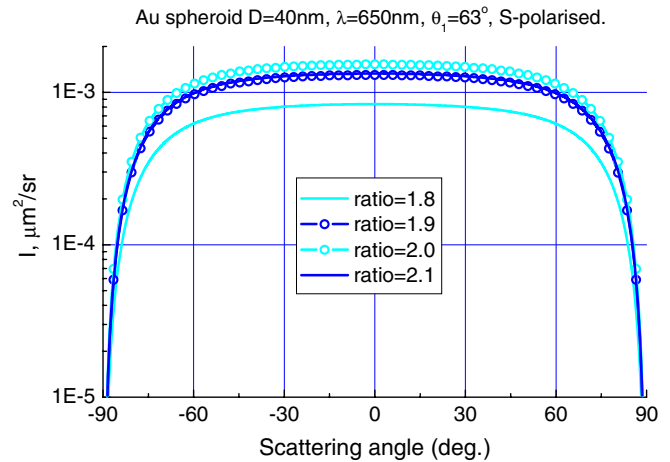


Fig. 12. The scattering intensity S-polarized component versus scattering angle for a spheroid of different aspect ratios,  $\lambda = 650$  nm.

2. The spectral peak value increases when vector  $E$  is parallel to the longer axis of a spheroid. An excitation of the longitude mode [12] is responsible for this effect.
3. The spectral peak reaches its maximum value for a spheroid of aspect ratio  $a = 2$ .

## 5. Conclusion

In this paper DSM has been applied to the scattering analysis of nanorod deposited on a prism surface. The main goal of the investigation was to clarify the scattering behaviour of nanorods on their aspect ratio and orientation with respect to an excitation. The results obtained by simulations allow to conclude that an aspect ratio  $a = 2$  provides the maximum value of the scattered field enhancement. It has been found that the response increases when the incident plane rotates from  $180^\circ$  to  $90^\circ$  and the main contribution into scattering enhancement was provided by the S-component of the incident light. The longitude mode is responsible for this enhancement.

## Acknowledgements

We gratefully acknowledge funding of this research by Deutsche Forschungsgemeinschaft (DFG) and the Russian Foundation for Basic Research (RFBR).

## References

- [1] U. Kreibig, M. Vollmer, *Optical Properties of Metal Clusters*, Springer, Berlin, Germany, 1995.
- [2] L.R. Hirsch, J.B. Jackson, A. Lee, N.J. Halas, J.L. West, A whole blood immunoassay using gold nanoshells, *Anal. Chem.* 75 (2003) 2377.
- [3] L. Ren, G.M. Chow, Synthesis of nir-sensitive Au–Au<sub>2</sub>S nanocolloids for drug delivery, *Materials Science and Engineering C23* (2003) 113.
- [4] C. Sönnichsen, A.P. Alivisatos, Gold nanorods as novel nonbleaching plasmon-based orientation sensors for polarized single-particle microscopy, *Nanoletters* 5 (2) (2005) 301.
- [5] J. Aizpurua, G.W. Bryant, L.J. Richter, F.J.G. de Abajo, B.K. Kelley, T. Mallouk, Optical properties of coupled metallic nanorods for field-enhanced spectroscopy, *Phys. Rev. B* 71 (2005) 235420.

- [6] J.K. Lim, K. Imura, T. Nagahara, S.K. Kim, H. Okamoto, Imaging and dispersion relations of surface Plasmon modes in silver nanorods by near-field spectroscopy, *Chem. Phys. Lett.* 412 (2005) 41.
- [7] J.J. Mock, D.R. Smith, S. Schultz, Local refractive index dependence of plasmon resonance spectra from individual nanoparticles, *Nano-letters* 3 (4) (2003) 485.
- [8] C. Sönnichsen, T. Franzl, T. Wilk, G. von Plessen, J. Feldmann, Drastic reduction of plasmon damping in gold nanorods, *Phys. Rev. Lett.* 88 (7) (2002) 077402-1.
- [9] E. Eremina, Y. Eremin, T. Wriedt, Discrete Sources Method for simulation of resonance spectra of nanoparticles on a plane surface, *Opt. Comm.* 246 (2005) 405.
- [10] O.P. Varnavski, M.B. Mohamed, M.A. El-Sayed, T. Goodson III, Relative enhancement of ultrafast emission in gold nanorods, *J. Phys. Chem. B* 107 (2003) 3101.
- [11] K.-S. Lee, M.A. El-Sayed, Dependence of the enhanced optical scattering efficiency relative to that of absorption for gold metal nanorods on aspect ratio, size, end-cap shape, and medium refractive index, *J. Phys. Chem. B* 109 (2005) 20331.
- [12] K. Imura, T. Nagahara, H. Okamoto, Near-field two-photon-induced photoluminescence from single gold nanorods and imaging of plasmon modes, *J. Phys. Chem. B* 109 (2005) 13214.
- [13] A. Brioude, X.C. Jiang, M.P. Pileni, Optical properties of gold nanorods: DDA simulations supported by experiments, *J. Phys. Chem. B* 109 (2005) 13138.
- [14] M. Futamata, Y. Maruyama, M. Ishikawa, Local electric field and scattering cross section of Ag nanoparticles under surface plasmon resonance by finite difference time domain method, *J. Phys. Chem. B* 107 (2003) 7607.
- [15] R. Ruppin, Polariton modes of spheroidal microcrystals, *J. Phys. Condens. Matter* 10 (1998) 7869.
- [16] Yu.A. Eremin, The method of discrete sources in electromagnetic scattering by axially symmetric structures, *J. Comm. Technol. Electron.* 45 (2) (2000) 269.
- [17] E. Eremina, Y. Eremin, T. Wriedt, Simulations of light scattering spectra of a nanoshell on plane interface based on the discrete sources method, *Opt. Comm.* 267 (2) (2006) 524.
- [18] D. Colton, R. Kress, *Inverse Acoustic and Electromagnetic Scattering Theory*, Springer, Berlin, 1992.
- [19] Y. Eremin, N. Orlov, A. Sveshnikov, in: T. Wriedt (Ed.), *Generalized Multipole Techniques for Electromagnetic and Light Scattering*, Elsevier Science, Amsterdam, 1999, p. 39.
- [20] A. Doicu, Yu. Eremin, T. Wriedt, *Acoustic and Electromagnetic Scattering Analysis using Discrete Sources*, Academic Press, London, 2000.
- [21] Yu.A. Eremin, J.C. Stover, N.V. Grishina, Discrete Sources Method for Light scattering analysis from 3D asymmetrical features on a substrate, *JQRST* 70 (4-6) (2001) 421.
- [22] Y. Eremin, N. Orlov, A. Sveshnikov, in: T. Wriedt (Ed.), *Generalized Multipole Techniques for Electromagnetic and Light Scattering*, Elsevier Science, Amsterdam, 1999, p. 39.